

# Physics-Informed Long-Range Coulomb Correction for Machine-learning Hamiltonians

Yang Zhong,<sup>1,\*</sup> Xiwen Li,<sup>1</sup> Xingao Gong,<sup>1</sup> and Hongjun Xiang<sup>1,†</sup>

<sup>1</sup>*Key Laboratory of Computational Physical Sciences (Ministry of Education),  
Institute of Computational Physical Sciences, State Key Laboratory of Surface Physics,  
and Department of Physics, Fudan University, Shanghai, 200433, China.*

Machine-learning electronic Hamiltonians achieve orders-of-magnitude speedups over density-functional theory, yet current models omit long-range Coulomb interactions that govern physics in polar crystals and heterostructures. We derive closed-form long-range Hamiltonian matrix elements in a nonorthogonal atomic-orbital basis through variational decomposition of the electrostatic energy, deriving a variationally consistent mapping from the electron density matrix to effective atomic charges. We implement this framework in HamGNN-LR, a dual-channel architecture combining E(3)-equivariant message passing with reciprocal-space Ewald summation. Benchmarks demonstrate that physics-based long-range corrections are essential: purely data-driven attention mechanisms fail to capture macroscopic electrostatic potentials. Benchmarks on polar ZnO slabs, CdSe/ZnS heterostructures, and GaN/AlN superlattices show two- to threefold error reductions and robust transferability to systems far beyond training sizes, eliminating the characteristic staircase artifacts that plague short-range models in the presence of built-in electric fields.

## I. INTRODUCTION

Accurate electronic-structure calculations underpin condensed-matter physics and materials science. Despite the success of density functional theory (DFT) [1, 2], self-consistent field (SCF) iterations entail prohibitive computational cost for large or complex systems. Machine-learning electronic Hamiltonians offer a transformative alternative [3–8]: by mapping atomic configurations directly to Hamiltonian matrix elements, these models bypass the SCF loop and achieve orders-of-magnitude speedups while preserving first-principles accuracy. Yet prevailing approaches invoke the nearsightedness principle [9], confining information flow to local atomic neighborhoods. This approximation breaks down in systems governed by long-range Coulomb interactions, including polar crystals, low-dimensional materials, and heterostructures, in which charge transfer, built-in electric fields, and macroscopic polarization arise from electrostatic interactions that extend far beyond any local cutoff.

In the development of machine-learning interatomic potentials, long-range interactions have been incorporated through charge equilibration [10], Gaussian charge representations [11], Ewald summation for  $1/r$  Coulomb tails [12], Fourier convolutions [13], and reciprocal-space neural networks [14]. These techniques target scalar potential energy surfaces and do not extend to electronic Hamiltonian matrices, which are tensorial matrix quantities constrained by E(3) equivariance and time-reversal symmetry. The mathematical structure required to encode long-range physics in Hamiltonians thus differs fundamentally from that in potential models.

We present a rigorous framework for incorporating long-range Coulomb interactions into Machine-learning

electronic Hamiltonians in a nonorthogonal atomic-orbital (NAO) basis. Through variational decomposition of the electrostatic energy into short- and long-range contributions, we derive closed-form expressions for long-range Hamiltonian matrix elements that ensure exact consistency between the Hamiltonian and total energy. This reciprocal-space formulation enables efficient evaluation via rapidly convergent  $k$ -space sums and systematic treatment of polar crystals and heterostructures.

## II. RESULTS

We decompose the total energy as  $E_{\text{tot}} = E_{\text{sr}} + E_{\text{lr}}$ , isolating the slowly convergent Coulomb tail into a reciprocal-space contribution [15]. With cutoff wave vector  $k_c$  and Gaussian smoothing width  $\sigma$ , the long-range electrostatic energy is

$$E_{\text{lr}} = \frac{1}{2\epsilon_0 V} \sum_{0 < |\mathbf{k}| < k_c} \frac{1}{k^2} \exp(-\sigma^2 k^2 / 2) |S(\mathbf{k})|^2, \quad (1)$$

where  $V$  is the unit-cell volume,  $\epsilon_0$  the vacuum permittivity, and  $S(\mathbf{k}) = \sum_i Q_i \exp(i\mathbf{k} \cdot \boldsymbol{\tau}_i)$  is the structure factor of net atomic charges  $Q_i$  at site  $i$ . To evaluate Eq. (1), we require the net atomic charges  $Q_i = Z_i - q_i$ , where  $q_i$  is the electronic population on atom  $i$ . We obtain  $q_i$  by integrating the electron density  $\rho(\mathbf{r})$  against a spatially localized weight function centered on atom  $i$ , following density-based population analysis [16, 17]:

$$q_i = \int W_i(\mathbf{r} - \boldsymbol{\tau}_i) \rho(\mathbf{r}) \, d\mathbf{r}.$$

In a nonorthogonal atomic-orbital (NAO) basis,  $\rho(\mathbf{r}) = \sum_{\mu\nu} P_{\mu\nu} \phi_\mu^*(\mathbf{r}) \phi_\nu(\mathbf{r})$ , so  $q_i = \sum_{\mu\nu} P_{\mu\nu} W_{i,\mu\nu}$  with orbital-projected weight-matrix elements

$$W_{i,\mu\nu} \equiv \int W_i(\mathbf{r} - \boldsymbol{\tau}_i) \phi_\mu^*(\mathbf{r}) \phi_\nu(\mathbf{r}) \, d\mathbf{r} = \frac{\partial q_i}{\partial P_{\mu\nu}}.$$

\* yzhong@fudan.edu.cn

† hxiang@fudan.edu.cn

Since  $Z_i$  is constant, we have  $\partial Q_i / \partial P_{\mu\nu} = -W_{i,\mu\nu}$ . The long-range Hamiltonian matrix elements follow from the chain rule:

$$H_{\text{lr},\mu\nu} = \frac{\partial E_{\text{lr}}}{\partial P_{\mu\nu}} = \sum_i \frac{\partial E_{\text{lr}}}{\partial Q_i} \frac{\partial Q_i}{\partial P_{\mu\nu}}, \quad (2)$$

where  $\partial E_{\text{lr}} / \partial Q_i$  is obtained by differentiating  $|S(\mathbf{k})|^2$ ; since  $\partial S / \partial Q_i = \exp(i\mathbf{k} \cdot \boldsymbol{\tau}_i)$ , the cross terms yield  $2 \text{Re}[S(\mathbf{k}) \exp(-i\mathbf{k} \cdot \boldsymbol{\tau}_i)]$  (Appendix A). For a real-valued NAO basis, always available when time-reversal symmetry holds,  $W_{i,\mu\nu}$  is real. Substituting into Eq. (2) and converting to atomic units ( $4\pi\epsilon_0 = 1$ ) yields the closed-form result:

$$H_{\text{lr},\mu\nu} = -\frac{4\pi}{V} \sum_{0 < |\mathbf{k}| < k_c} \frac{\exp(-\sigma^2 k^2 / 2)}{k^2} \times \text{Re} \left[ S(\mathbf{k}) \sum_i \exp(-i\mathbf{k} \cdot \boldsymbol{\tau}_i) W_{i,\mu\nu} \right]. \quad (3)$$

Equation (3) couples the macroscopic field carried by  $S(\mathbf{k})$  to the orbital-projected weight matrix  $W_{i,\mu\nu}$ , ensuring variational consistency— $H_{\text{lr},\mu\nu} = \partial E_{\text{lr}} / \partial P_{\mu\nu}$ —by construction. The Ewald self-interaction energy  $E_{\text{self}} \propto \sum_i Q_i^2$  [18, 19] generates a spatially local correction  $\partial E_{\text{self}} / \partial P_{\mu\nu} \propto \sum_i Q_i W_{i,\mu\nu}$  that lies within the short-range receptive field and is absorbed into  $H_{\text{sr}}$  (Appendix A 5). Expanding  $S(\mathbf{k}) = \sum_j Q_j e^{i\mathbf{k} \cdot \boldsymbol{\tau}_j}$  shows that the bracketed factor in Eq. (3) reduces to  $\text{Re}[\sum_{i,j} Q_j W_{i,\mu\nu} e^{-i\mathbf{k} \cdot (\boldsymbol{\tau}_i - \boldsymbol{\tau}_j)}]$ , a pairwise sum whose phases depend solely on relative displacements  $\boldsymbol{\tau}_i - \boldsymbol{\tau}_j$ . This structure is directly exploited by the Ewald attention module described below.

Guided by this analytic form, we construct HamGNN-LR (Fig. 1), a dual-channel architecture separating short- and long-range physics. The short-range channel employs E(3)-equivariant message passing for local bonding and orbital hybridization [7, 20], producing equivariant node features  $\mathbf{h}_i^{\text{sr}}$ . The long-range channel—an *Ewald attention module*—operates in reciprocal space to capture macroscopic electrostatic correlations beyond the real-space cutoff, and ultimately evaluates  $H_{\text{lr}}$  via Eq. (3). The two channels are merged through a gated residual connection  $\mathbf{h}_i^{\text{lr}} \leftarrow (1 - \alpha) \mathbf{h}_i^{\text{sr}} + \alpha \text{EquivariantNonlin}(\mathbf{h}_i^{\text{sr}})$  with learnable gate  $\alpha$ , ensuring that the long-range correction is introduced as a small perturbation to the short-range baseline during early training.

The Ewald attention module is designed to reproduce the pairwise phase structure  $\mathbf{k}_m \cdot (\boldsymbol{\tau}_i - \boldsymbol{\tau}_j)$  that appears in Eq. (3). We sample a discrete set of wave vectors  $\{\mathbf{k}_m\}$  with  $|\mathbf{k}_m| < k_c$  from the reciprocal lattice. For each  $\mathbf{k}_m$ , invariant scalar components of the node features are projected into query and key vectors, to which rotary position encoding (RoPE) [21] is applied with phase  $\theta_{j,m} = \mathbf{k}_m \cdot \boldsymbol{\tau}_j$ . The resulting inner product  $\langle \tilde{\mathbf{q}}_{i,m}, \tilde{\mathbf{k}}_{j,m} \rangle$  depends solely on the relative displacement phase  $\mathbf{k}_m \cdot (\boldsymbol{\tau}_i - \boldsymbol{\tau}_j)$ , exactly matching the Ewald

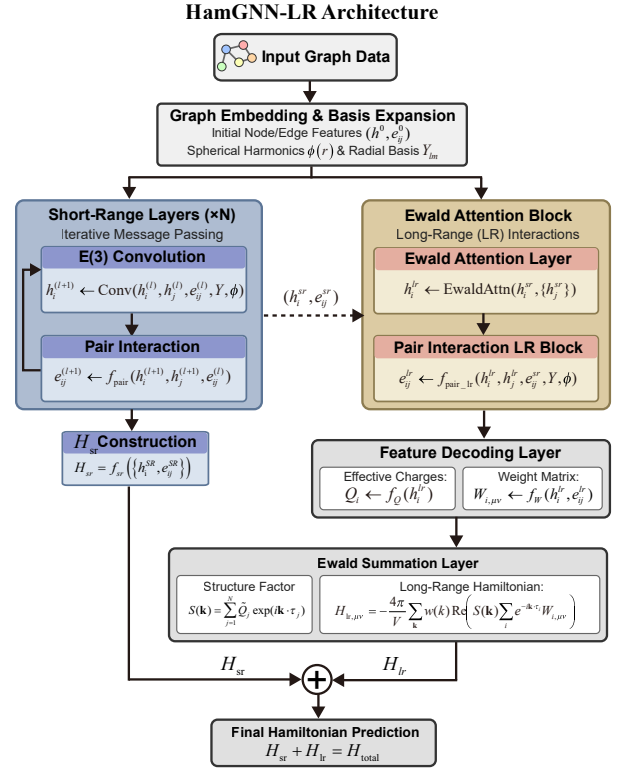


FIG. 1. Architecture of HamGNN-LR for predicting  $H_{\text{total}} = H_{\text{sr}} + H_{\text{lr}}$ . Short-range E(3)-equivariant message passing constructs  $H_{\text{sr}}$  from local environments. An Ewald attention module captures long-range correlations in reciprocal space with  $\mathcal{O}(N|\mathcal{K}|)$  cost, linear in system size  $N$  for fixed sampled wave vectors  $|\mathcal{K}|$ , and decodes ionic charges  $Q_i$  and weight matrices  $W_{i,\mu\nu}$ . The decoded charges are neutralized ( $Q_j \mapsto \tilde{Q}_j$ ) and, together with the weight matrices  $W_{i,\mu\nu}$ , substituted into the analytic correction  $H_{\text{lr}}$  [Eq. (3)].

summation kernel. The value vectors carry full equivariant content and are aggregated via linearized attention—first summing over atoms at each  $\mathbf{k}_m$ , then over wave vectors—yielding  $\mathcal{O}(N|\mathcal{K}|)$  complexity, linear in system size  $N$  for a fixed reciprocal grid, versus  $\mathcal{O}(N^2)$  for standard all-pairs attention. The aggregated features  $\mathbf{h}_i^{\text{lr}}$  inherit E(3) equivariance because only invariant scalars participate in RoPE and attention weights, while the equivariant value vectors pass through unrotated.

From the updated long-range node features  $\mathbf{h}_i^{\text{lr}}$ , the module decodes effective ionic charges  $Q_i$  via an invariant readout. Since network-predicted charges need not satisfy global neutrality, we apply a zero-mean projection  $\tilde{Q}_j = Q_j - N^{-1} \sum_k Q_k$  before Ewald summation, defining the structure factor

$$S(\mathbf{k}_m) = \frac{1}{N} \sum_{j=1}^N \tilde{Q}_j \exp(i\mathbf{k}_m \cdot \boldsymbol{\tau}_j), \quad (4)$$

where the  $1/N$  prefactor renders  $S(\mathbf{k}_m)$  an intensive quantity consistent with the  $1/V$  normalization in Eq. (1). Long-range edge features  $\mathbf{e}_{ij}^{\text{lr}}$  are constructed

by concatenating node features of the two endpoints and coupling them to spherical-harmonic embeddings of the bond direction via Clebsch–Gordan tensor products, injecting directional information while preserving equivariance. The weight matrices  $W_{i,\mu\nu}$  are then decoded from the node features (onsite elements) and edge features (offsite elements). Finally,  $\tilde{Q}_j$  and  $W_{i,\mu\nu}$  are substituted into Eq. (3) to yield  $H_{\text{lr}}$ , giving the total prediction  $H_{\mu\nu} = H_{\text{sr},\mu\nu} + H_{\text{lr},\mu\nu}$ .

Unlike prior reciprocal-space attention schemes [12, 22–24], which target scalar energy predictions, this construction is grounded in the analytic Hamiltonian expression [Eq. (3)], preserves E(3) equivariance at every stage, and scales linearly in  $N$ . Additional implementation details—including Q/K/V projections, the RoPE convention, linearized aggregation, and the gated residual connection—are given in Appendix B.

To disentangle the effect of the explicit long-range correction from that of increased network capacity, we restrict all models to a single interaction layer, confining the receptive field to minimal local neighborhoods. We compare four variants that systematically include or exclude two key ingredients: the physics-based  $H_{\text{lr}}$  [Eq. (3)] and the Ewald attention module: (i) **SR**, a short-range baseline with neither; (ii) **LR-loc**, which evaluates  $H_{\text{lr}}$  via Eq. (3) but decodes  $Q_i$  and  $W_{i,\mu\nu}$  from the short-range node and edge features alone, without Ewald attention; (iii) **LR-EA** (full HamGNN-LR), which first extracts long-range features through Ewald attention, decodes  $Q_i$  and  $W_{i,\mu\nu}$  from the resulting long-range node and edge features, and evaluates  $H_{\text{lr}}$ ; and (iv) **EA**, which incorporates Ewald attention to augment node features but omits the physics-based  $H_{\text{lr}}$  term, relying entirely on the network to learn long-range effects in a data-driven manner. Table I reports Hamiltonian mean absolute error (MAE) on three polar/heterostructure systems—ZnO slab, GaN/AlN superlattice, and CdSe/ZnS heterostructure—each split 60%/20%/20% for training/validation/test.

Incorporating the physics-based correction proves decisive. In CdSe/ZnS, LR-EA reduces test MAE from 3.279 meV (SR) to 1.058 meV—a threefold improvement—while even LR-loc, which lacks reciprocal-space feature extraction, reaches 1.292 meV; in GaN/AlN, LR-EA similarly reduces test MAE from 3.646 meV to 1.162 meV. By contrast, EA—equipped with Ewald attention but lacking the analytic Hamiltonian term—yields 3.158 meV in CdSe/ZnS and 3.598 meV in GaN/AlN, essentially identical to the short-range baseline. In all three tested systems, EA provides negligible improvement, confirming that data-driven attention alone, without the physics-based Hamiltonian correction, is insufficient to capture macroscopic electrostatic effects within a single-layer architecture. Both LR-loc and LR-EA reduce errors by factors of two to three, demonstrating that the explicit, variationally consistent  $H_{\text{lr}}$  is the essential ingredient; Ewald attention further enhances accuracy by providing long-range-aware features for decod-

ing  $Q_i$  and  $W_{i,\mu\nu}$ . Nevertheless, the truncated Coulomb tail is recovered by the physics-based correction rather than by the attention mechanism per se.

TABLE I. Hamiltonian MAE (meV) for single-layer models on three polar/heterostructure systems. SR: short-range baseline; LR-loc: long-range correction [Eq. (3)] with local decoding; LR-EA: full HamGNN-LR (correction + Ewald attention); EA: Ewald attention only, without physics-based  $H_{\text{lr}}$ .

System	Split	SR	LR-loc	LR-EA	EA
ZnO slab	Train	1.278	0.685	0.596	1.099
	Test	1.336	0.747	0.635	1.153
GaN/AlN	Train	3.623	1.462	1.184	3.556
	Test	3.646	1.313	1.162	3.598
CdSe/ZnS	Train	3.380	1.311	1.057	3.231
	Test	3.279	1.292	1.058	3.158

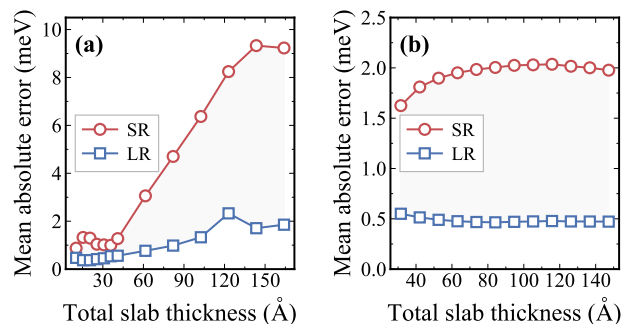


FIG. 2. Hamiltonian MAE of single-layer SR (red circles) and LR (blue squares) models versus layer thickness for (a) GaN/AlN superlattices and (b) polar ZnO slabs. In (a), SR error grows with superlattice period and saturates at  $\sim 140$  Å; in (b), SR error rises with slab thickness before leveling off. The LR model [Eq. (3)] maintains uniformly low errors across all thicknesses.

To examine size dependence, we evaluate single-layer SR and LR models as a function of layer thickness in GaN/AlN superlattices and polar ZnO slabs (Fig. 2). In both systems, SR error rises with thickness: in GaN/AlN it grows with superlattice period and saturates at  $\sim 140$  Å; in ZnO it increases with slab thickness before leveling off. The macroscopic built-in field, originating from bound polarization charges at interfaces (GaN/AlN) or spontaneous polarization along the  $c$  axis (ZnO), produces an electrostatic potential that grows linearly beyond the single-layer receptive field. The LR model maintains uniformly low errors across all thicknesses, with only a mild increase at the largest sizes; even at maximum thickness, LR error remains below SR error at minimum thickness. This confirms that reciprocal-space Ewald correction in Eq. (3) successfully restores the macroscopic electrostatic potential discarded by real-space truncation.

We next benchmark HamGNN-LR against three representative short-range models—DeepH-E3 [6], DeePTB-

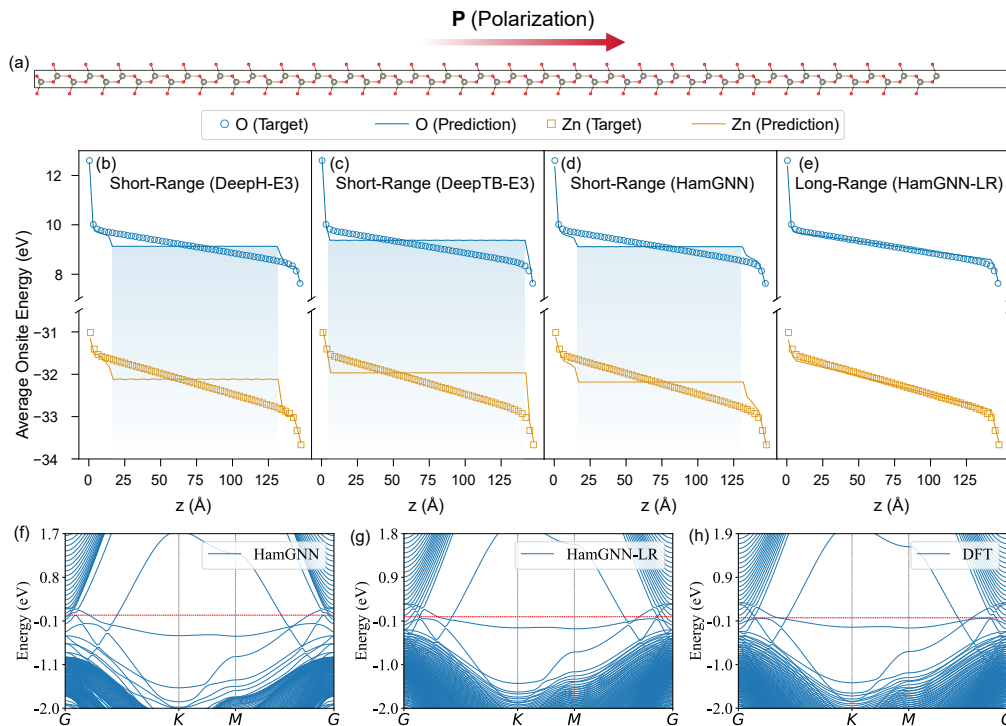


FIG. 3. Real-space onsite energy and band structure of the 56-layer polar ZnO slab. (a) Structural schematic; red arrow denotes spontaneous polarization  $\mathbf{P}$ . (b)–(e) Spatially resolved average onsite Hamiltonian matrix elements along  $z$  for (b) DeepH-E3, (c) DeePTB-E3, (d) short-range HamGNN, and (e) HamGNN-LR. Open symbols: DFT reference; solid lines: model predictions. Shaded regions in (b)–(d) highlight staircase discontinuities arising from finite receptive fields; these artifacts are absent in (e) owing to the long-range correction. (f)–(h) Band structures along  $\Gamma$ – $K$ – $M$ – $\Gamma$  for (f) short-range HamGNN, (g) HamGNN-LR, and (h) DFT reference. Dashed red lines mark the Fermi level. HamGNN-LR closely reproduces DFT bands, whereas the short-range model exhibits visible deviations near the band gap.

E3 [8], and HamGNN [7, 20]—all using three interaction layers. Beyond standard train/test evaluation on ZnO slabs, we perform a stringent size-extrapolation test: models trained on thinner slabs predict the Hamiltonian of a 56-layer ZnO slab far outside the training distribution (Table II).

TABLE II. Hamiltonian MAE (meV) for three-layer models on ZnO slabs. “ZnO (thick)” denotes size extrapolation to a 56-layer (147.25 Å) slab unseen during training.

Split	DeepH-E3	DeePTB-E3	HamGNN	HamGNN-LR
Train	0.462	1.940	0.397	<b>0.291</b>
Test	0.578	2.450	0.538	<b>0.349</b>
ZnO (thick)	1.525	2.383	1.565	<b>0.473</b>

On the standard test set, HamGNN-LR achieves the lowest error (0.349 meV), a 35% reduction over HamGNN (0.538 meV) and 40% over DeepH-E3 (0.578 meV). This confirms that the long-range correction yields substantial gains even when the receptive field already spans three interaction layers. The advantage is most pronounced under size extrapolation: errors of all short-range models increase sharply—to 1.525 meV (+164%) for DeepH-E3 and 1.565 meV (+191%) for HamGNN—

whereas HamGNN-LR reaches only 0.473 meV (+36%). This robust extrapolation stems directly from Eq. (3): Ewald summation analytically captures the macroscopic spontaneous-polarization field along the  $c$  axis, whose spatial extent grows linearly with slab thickness. No practically feasible number of message-passing layers can reproduce this behavior.

Figure 3 provides a microscopic view of the long-range correction on the 56-layer ZnO slab. In the DFT reference, onsite energies of both O and Zn atoms vary nearly linearly along  $z$ , reflecting the macroscopic electrostatic potential gradient generated by the spontaneous polarization. All three short-range models [Figs. 3(b)–(d)] exhibit characteristic staircase artifacts: within each receptive-field window local chemistry is captured correctly, but the model cannot account for the electrostatic potential increment  $\Delta\phi$  accumulated beyond the cutoff radius. The step width corresponds to the effective range of three message-passing layers, and the cumulative mismatch grows with  $z$ , consistent with the increasing errors reported in Table II. HamGNN-LR [Fig. 3(e)] eliminates these artifacts entirely. Ewald summation restores the continuous linear potential gradient by incorporating the small- $|\mathbf{k}|$  components of  $S(\mathbf{k})$  that encode the macroscopic charge distribution. This advantage is mir-

rored in reciprocal space. The short-range band structure [Fig. 3(f)] misplaces both valence- and conduction-band edges and distorts their curvature, yielding an underestimated band gap and spurious splittings of low-lying subbands along the high-symmetry path. In contrast, HamGNN-LR [Fig. 3(g)] closely reproduces the DFT reference [Fig. 3(h)]: band extrema, near-gap ordering, and curvature at  $\Gamma$  and  $M$  are all faithfully captured, confirming that long-range Ewald correction is essential for quantitative band-structure accuracy in polarized slabs.

### III. CONCLUSION

We have derived closed-form, variationally consistent long-range Hamiltonian matrix elements [Eq. (3)] in a nonorthogonal atomic-orbital basis and implemented them within HamGNN-LR, a framework that incorpo-

rates macroscopic Coulomb fields into Machine-learning electronic Hamiltonians. Single-layer ablation demonstrates that the explicit long-range correction is decisive in polar and heterostructure systems, whereas data-driven attention alone fails to reproduce long-range electrostatic effects. HamGNN-LR maintains low errors under size extrapolation to thick ZnO slabs outside the training distribution. Analysis of real-space onsite energy profiles traces the staircase artifacts of short-range models to truncated built-in fields and confirms that the long-range correction restores continuous potential gradients. These results demonstrate that analytical, variationally consistent long-range Coulomb corrections are essential for accurate, cross-scale Machine-learning electronic-structure predictions in polar materials and heterostructures. The framework opens a pathway toward accurate, large-scale electronic-structure modeling of interfaces, superlattices, and other systems in which long-range electrostatic effects are dominant.

- 
- [1] R. O. Jones, Density functional theory: Its origins, rise to prominence, and future, *Rev. Mod. Phys.* **87**, 897 (2015).
- [2] A. D. Becke, Perspective: Fifty years of density-functional theory in chemical physics, *J. Chem. Phys.* **140**, 18A301 (2014).
- [3] K. T. Schütt, M. Gastegger, A. Tkatchenko, K.-R. Müller, and R. J. Maurer, Unifying machine learning and quantum chemistry with a deep neural network for molecular wavefunctions, *Nat. Commun.* **10**, 5024 (2019).
- [4] O. T. Unke, S. Chmiela, M. Gastegger, K. T. Schütt, H. E. Sauceda, and K.-R. Müller, SE(3)-equivariant prediction of molecular wavefunctions and electronic densities, *Adv. Neural Inf. Process. Syst.* **34**, 14434 (2021).
- [5] H. Li, Z. Wang, N. Zou, M. Ye, R. Xu, X. Gong, W. Duan, and Y. Xu, Deep-learning density functional theory Hamiltonian for efficient ab initio electronic-structure calculation, *Nat. Comput. Sci.* **2**, 367 (2022).
- [6] X. Gong, H. Li, N. Zou, R. Xu, W. Duan, and Y. Xu, General framework for E(3)-equivariant neural network representation of density functional theory Hamiltonian, *Nat. Commun.* **14**, 2848 (2023).
- [7] Y. Zhong, H. Yu, M. Su, X. Gong, and H. Xiang, Transferable equivariant graph neural networks for the Hamiltonians of molecules and solids, *npj Comput. Mater.* **9**, 182 (2023).
- [8] Z. Zhouyin, Z. Gan, M. Liu, S. K. Pandey, L. Zhang, and Q. Gu, Learning local equivariant representations for quantum operators, in *International Conference on Learning Representations (ICLR)* (2025) [arXiv:2407.06053 \[cond-mat.mtrl-sci\]](https://arxiv.org/abs/2407.06053).
- [9] E. Prodan and W. Kohn, Nearsightedness of electronic matter, *Proc. Natl. Acad. Sci. U.S.A.* **102**, 11635 (2005).
- [10] T. W. Ko, J. A. Finkler, S. Goedecker, and J. Behler, A fourth-generation high-dimensional neural network potential with accurate electrostatics including non-local charge transfer, *Nat. Commun.* **12**, 398 (2021).
- [11] L. Zhang, H. Wang, M. C. Muniz, A. Z. Panagiotopoulos, R. Car, and W. E, Deep potential long-range, *J. Chem. Phys.* **156**, 124107 (2022).
- [12] A. Kosmala, J. Gasteiger, N. Gao, and S. Günnemann, Ewald-based long-range message passing for molecular graphs, in *Proceedings of the 40th International Conference on Machine Learning (ICML)*, Proceedings of Machine Learning Research, Vol. 202 (PMLR, 2023) pp. 17544–17563.
- [13] A. Grisafi and M. Ceriotti, Incorporating long-range physics in atomic-scale machine learning, *J. Chem. Phys.* **151**, 204105 (2019).
- [14] H. Yu, L. Hong, S. Chen, X. Gong, and H. Xiang, Capturing long-range interaction with reciprocal space neural network (2022), [arXiv:2211.16684 \[cond-mat.mtrl-sci\]](https://arxiv.org/abs/2211.16684).
- [15] P. P. Ewald, Die berechnung optischer und elektrostatischer gitterpotentiale, *Ann. Phys.* **369**, 253 (1921).
- [16] F. L. Hirshfeld, Bonded-atom fragments for describing molecular charge densities, *Theoret. Chim. Acta* **44**, 129 (1977).
- [17] A. D. Becke, A multicenter numerical integration scheme for polyatomic molecules, *J. Chem. Phys.* **88**, 2547 (1988).
- [18] A. Y. Toukmaji and J. A. Board, Ewald summation techniques in perspective: A survey, *Comput. Phys. Commun.* **95**, 73 (1996).
- [19] S. W. de Leeuw, J. W. Perram, and E. R. Smith, Simulation of electrostatic systems in periodic boundary conditions. I. Lattice sums and dielectric constants, *Proc. R. Soc. Lond. A* **373**, 27 (1980).
- [20] Y. Zhong, R. Wang, X. Gong, and H. Xiang, A universal spin-orbit-coupled Hamiltonian model for accelerated quantum material discovery, *Nat. Mach. Intell.* **10.1038/s42256-026-01196-x** (2026), [arXiv:2504.19586 \[cond-mat.mtrl-sci\]](https://arxiv.org/abs/2504.19586).
- [21] J. Su, Y. Lu, S. Pan, A. Murtadha, B. Wen, and Y. Liu, Roformer: Enhanced transformer with rotary position embedding, *Neurocomputing* **568**, 127063 (2024), [arXiv:2104.09864 \[cs.CL\]](https://arxiv.org/abs/2104.09864).
- [22] J. T. Frank, S. Chmiela, K.-R. Müller, and O. T. Unke, Euclidean fast attention: Machine learning global atomic representations at linear cost (2024), [arXiv:2412.08541](https://arxiv.org/abs/2412.08541)

[cs.LG].

- [23] E. Qu, B. M. Wood, A. S. Krishnapriyan, and Z. W. Ulissi, A recipe for scalable attention-based MLPs: unlocking long-range accuracy with all-to-all node attention (2026), [arXiv:2603.06567 \[physics.chem-ph\]](#).
- [24] A. Caruso, J. Venturin, L. Giambagli, E. Rolando, F. Noé, and C. Clementi, Extending the RANGE of graph neural networks: Relaying attention nodes for global encoding (2025), [arXiv:2502.13797 \[cs.LG\]](#).

## Appendix A: Derivation of the Long-Range Hamiltonian Correction

This appendix provides a self-contained derivation of the long-range Hamiltonian matrix elements  $H_{\text{lr},\mu\nu}$  stated in Eq. (3). The strategy is as follows. The reciprocal-space electrostatic energy  $E_{\text{lr}}$  depends on the density matrix  $P_{\mu\nu}$  only through the net atomic charges  $\{Q_i\}$ . Applying the variational principle  $H_{\text{lr},\mu\nu} = \partial E_{\text{lr}}/\partial P_{\mu\nu}$  therefore reduces, via the chain rule, to evaluating two factors: (i) the *density-matrix sensitivity*  $\partial Q_i/\partial P_{\mu\nu}$ , which encodes how atomic charges respond to changes in the density matrix, and (ii) the *electrostatic response*  $\partial E_{\text{lr}}/\partial Q_i$ , which gives the long-range potential at each atomic site. We derive each factor in turn and then combine them into a closed-form expression.

### 1. Variational Framework and Chain Rule

The long-range electrostatic energy with Gaussian-smoothed reciprocal-space cutoff is [Eq. (1)]

$$E_{\text{lr}} = \frac{1}{2\epsilon_0 V} \sum_{0 < |\mathbf{k}| < k_c} \frac{1}{k^2} e^{-\sigma^2 k^2/2} |S(\mathbf{k})|^2, \quad (\text{A1})$$

where  $V$  is the unit-cell volume,  $\epsilon_0$  the vacuum permittivity,  $\sigma$  the Gaussian smoothing width, and the structure factor

$$S(\mathbf{k}) = \sum_i Q_i e^{i\mathbf{k}\cdot\boldsymbol{\tau}_i} \quad (\text{A2})$$

encodes the net atomic charges  $Q_i \equiv Z_i - q_i$  ( $Z_i$ : nuclear charge;  $q_i$ : electronic population) at positions  $\boldsymbol{\tau}_i$ . We assume overall charge neutrality,  $\sum_i Q_i = 0$ , a prerequisite for the convergence of the Ewald sum in periodic systems and for the well-definedness of  $S(\mathbf{k})$  at small  $|\mathbf{k}|$ .

Because  $E_{\text{lr}}$  depends on  $P_{\mu\nu}$  only through  $\{Q_i\}$ , the variational principle yields

$$\begin{aligned} H_{\text{lr},\mu\nu} &= \frac{\partial E_{\text{lr}}}{\partial P_{\mu\nu}} \\ &= \sum_i \underbrace{\frac{\partial E_{\text{lr}}}{\partial Q_i}}_{\text{electrostatic response}} \underbrace{\frac{\partial Q_i}{\partial P_{\mu\nu}}}_{\text{density-matrix sensitivity}}. \end{aligned} \quad (\text{A3})$$

This equation serves as the roadmap for the remainder of the derivation. We evaluate the right-hand factor first (Sec. A2), then the left-hand factor (Sec. A3), and finally assemble the result (Sec. A4).

### 2. Density-Matrix Sensitivity: $\partial Q_i/\partial P_{\mu\nu}$

In a nonorthogonal atomic-orbital (NAO) basis  $\{\phi_\mu(\mathbf{r})\}$ , the single-particle density matrix  $P_{\mu\nu}$  determines the electron density

$$\rho(\mathbf{r}) = \sum_{\mu\nu} P_{\mu\nu} \phi_\mu^*(\mathbf{r}) \phi_\nu(\mathbf{r}). \quad (\text{A4})$$

The electronic population on atom  $i$  is obtained by projecting  $\rho(\mathbf{r})$  onto a spatially localized weight function  $W_i(\mathbf{r} - \boldsymbol{\tau}_i)$  [16, 17]:

$$q_i = \int W_i(\mathbf{r} - \boldsymbol{\tau}_i) \rho(\mathbf{r}) \, d\mathbf{r} = \sum_{\mu\nu} P_{\mu\nu} W_{i,\mu\nu}, \quad (\text{A5})$$

where the second equality follows from substituting Eq. (A4) and defining the orbital-projected weight-matrix elements

$$W_{i,\mu\nu} \equiv \int W_i(\mathbf{r} - \boldsymbol{\tau}_i) \phi_\mu^*(\mathbf{r}) \phi_\nu(\mathbf{r}) \, d\mathbf{r}. \quad (\text{A6})$$

Because  $Q_i = Z_i - q_i$  and  $Z_i$  is independent of  $P_{\mu\nu}$ , the desired sensitivity is

$$\frac{\partial Q_i}{\partial P_{\mu\nu}} = -\frac{\partial q_i}{\partial P_{\mu\nu}} = -W_{i,\mu\nu}. \quad (\text{A7})$$

For a real-valued NAO basis—which can always be chosen when time-reversal symmetry holds— $W_{i,\mu\nu}$  is real, a property that will be used when simplifying the final expression.

### 3. Electrostatic Response: $\partial E_{\text{lr}}/\partial Q_i$

To evaluate the second factor in Eq. (A3), we differentiate  $|S(\mathbf{k})|^2 = S(\mathbf{k}) S^*(\mathbf{k})$  with respect to  $Q_i$ . The product rule gives

$$\frac{\partial |S|^2}{\partial Q_i} = \frac{\partial S}{\partial Q_i} S^* + S \frac{\partial S^*}{\partial Q_i}. \quad (\text{A8})$$

From Eq. (A2),  $\partial S/\partial Q_i = e^{i\mathbf{k}\cdot\boldsymbol{\tau}_i}$  and  $\partial S^*/\partial Q_i = e^{-i\mathbf{k}\cdot\boldsymbol{\tau}_i}$ . Substituting and using  $z + z^* = 2\text{Re}(z)$  with  $z \equiv S(\mathbf{k}) e^{-i\mathbf{k}\cdot\boldsymbol{\tau}_i}$ :

$$\frac{\partial |S(\mathbf{k})|^2}{\partial Q_i} = 2 \text{Re}[S(\mathbf{k}) e^{-i\mathbf{k}\cdot\boldsymbol{\tau}_i}]. \quad (\text{A9})$$

Differentiating Eq. (A1) and noting that the factor  $\frac{1}{2}$  in  $E_{\text{lr}}$  cancels with the factor of 2 from Eq. (A9), we obtain

$$\frac{\partial E_{\text{lr}}}{\partial Q_i} = \frac{1}{\epsilon_0 V} \sum_{0 < |\mathbf{k}| < k_c} \frac{e^{-\sigma^2 k^2/2}}{k^2} \text{Re}[S(\mathbf{k}) e^{-i\mathbf{k}\cdot\boldsymbol{\tau}_i}]. \quad (\text{A10})$$

Physically, this quantity equals the long-range component of the electrostatic potential at site  $i$ , generated by the Gaussian-smoothed charge distribution of all other atoms in reciprocal space.

#### 4. Assembly and Final Result

We now substitute Eqs. (A7) and (A10) into the chain rule [Eq. (A3)]:

$$H_{\text{lr},\mu\nu} = -\frac{1}{\epsilon_0 V} \sum_{0 < |\mathbf{k}| < k_c} \frac{e^{-\sigma^2 k^2/2}}{k^2} \times \text{Re} \left[ S(\mathbf{k}) \sum_i e^{-i\mathbf{k} \cdot \boldsymbol{\tau}_i} W_{i,\mu\nu} \right]. \quad (\text{A11})$$

Because  $W_{i,\mu\nu}$  is real (Sec. A2), it can be moved inside the  $\text{Re}[\dots]$  operator, and the sum over atoms  $i$  can be performed under the same sign:

$$H_{\text{lr},\mu\nu} = -\frac{1}{\epsilon_0 V} \sum_{0 < |\mathbf{k}| < k_c} \frac{e^{-\sigma^2 k^2/2}}{k^2} \times \text{Re} \left[ S(\mathbf{k}) \sum_i e^{-i\mathbf{k} \cdot \boldsymbol{\tau}_i} W_{i,\mu\nu} \right]. \quad (\text{A12})$$

Converting to Hartree atomic units ( $4\pi\epsilon_0 = 1$ , hence  $1/\epsilon_0 = 4\pi$ ) yields the final closed-form expression:

$$H_{\text{lr},\mu\nu} = -\frac{4\pi}{V} \sum_{0 < |\mathbf{k}| < k_c} \frac{e^{-\sigma^2 k^2/2}}{k^2} \times \text{Re} \left[ S(\mathbf{k}) \sum_i e^{-i\mathbf{k} \cdot \boldsymbol{\tau}_i} W_{i,\mu\nu} \right], \quad (\text{A13})$$

which is Eq. (3) of the main text. By construction,  $H_{\text{lr},\mu\nu} = \partial E_{\text{lr}} / \partial P_{\mu\nu}$ , ensuring variational consistency between the long-range energy and Hamiltonian.

*a. Pairwise phase structure.* Expanding  $S(\mathbf{k}) = \sum_j Q_j e^{i\mathbf{k} \cdot \boldsymbol{\tau}_j}$  in Eq. (A13), the argument of  $\text{Re}[\dots]$  becomes

$$\sum_{i,j} Q_j W_{i,\mu\nu} e^{-i\mathbf{k} \cdot (\boldsymbol{\tau}_i - \boldsymbol{\tau}_j)}, \quad (\text{A14})$$

a sum over atom pairs  $(i, j)$  whose phase depends solely on the relative displacement  $\boldsymbol{\tau}_i - \boldsymbol{\tau}_j$ . This translational-invariant pairwise structure is the key property exploited by the Ewald attention module (Appendix B).

#### 5. Ewald Self-Interaction Correction

The reciprocal-space Ewald sum in Eq. (A1) implicitly includes the unphysical interaction of each point charge with its own Gaussian screening cloud [18, 19]. This self-interaction must be subtracted. We derive the corresponding Hamiltonian correction by the same variational chain-rule procedure used above.

*a. Self-interaction energy.* The Gaussian screening cloud centered on atom  $i$  has the normalized charge density

$$\rho_i^{\text{scr}}(\mathbf{r}) = \frac{Q_i}{(2\pi\sigma^2)^{3/2}} \exp\left(-\frac{|\mathbf{r} - \boldsymbol{\tau}_i|^2}{2\sigma^2}\right). \quad (\text{A15})$$

The electrostatic potential of this distribution, evaluated at its own center  $\mathbf{r} = \boldsymbol{\tau}_i$ , is

$$\phi_i^{\text{self}} = \frac{1}{4\pi\epsilon_0} \int \frac{\rho_i^{\text{scr}}(\mathbf{r})}{|\mathbf{r} - \boldsymbol{\tau}_i|} d^3\mathbf{r} = \frac{Q_i}{4\pi\epsilon_0} \sqrt{\frac{2}{\pi}} \frac{1}{\sigma}, \quad (\text{A16})$$

where the radial integral  $\int_0^\infty r e^{-r^2/(2\sigma^2)} dr = \sigma^2$  has been used. The total self-interaction energy, with the factor of  $\frac{1}{2}$  to avoid double counting, is

$$E_{\text{self}} = \frac{1}{2} \sum_i Q_i \phi_i^{\text{self}} = \frac{1}{4\pi\epsilon_0} \frac{1}{\sqrt{2\pi}\sigma} \sum_i Q_i^2. \quad (\text{A17})$$

*b. Variational Hamiltonian correction.* Differentiating Eq. (A17) with respect to  $Q_i$  gives  $\partial E_{\text{self}} / \partial Q_i = 2Q_i / (4\pi\epsilon_0 \sqrt{2\pi}\sigma)$ . Applying the chain rule  $H_{\text{self},\mu\nu} = \sum_i (\partial E_{\text{self}} / \partial Q_i) (\partial Q_i / \partial P_{\mu\nu})$  with  $\partial Q_i / \partial P_{\mu\nu} = -W_{i,\mu\nu}$  [Eq. (A7)] yields, after conversion to Hartree atomic units ( $4\pi\epsilon_0 = 1$ ),

$$H_{\text{self},\mu\nu} = -\frac{2}{\sqrt{2\pi}\sigma} \sum_i Q_i W_{i,\mu\nu}. \quad (\text{A18})$$

*c. Locality and absorption into  $H_{\text{sr}}$ .* In contrast to the reciprocal-space sum in  $H_{\text{lr},\mu\nu}$  [Eq. (A13)], the self-interaction correction Eq. (A18) is *spatially local*:  $W_{i,\mu\nu}$  is nonvanishing only for orbitals  $\mu, \nu$  within the compact support of the weight function centered on atom  $i$ , so  $H_{\text{self},\mu\nu}$  contributes only to onsite and near-neighbor matrix elements. The complete variationally consistent long-range Hamiltonian is

$$H_{\mu\nu}^{\text{lr,full}} = H_{\text{lr},\mu\nu} - H_{\text{self},\mu\nu}. \quad (\text{A19})$$

Because  $H_{\text{self},\mu\nu}$  lies entirely within the receptive field of the short-range message-passing network, it can equivalently be absorbed into the short-range channel  $H_{\text{sr}}$  during training. In either case, variational consistency is maintained:  $H_{\alpha,\mu\nu} = \partial E_\alpha / \partial P_{\mu\nu}$  holds for each component  $\alpha \in \{\text{sr}, \text{lr}, \text{self}\}$  independently, so

$$H_{\text{tot},\mu\nu} = H_{\text{sr},\mu\nu} + H_{\text{lr},\mu\nu} - H_{\text{self},\mu\nu} = \frac{\partial E_{\text{tot}}}{\partial P_{\mu\nu}} \quad (\text{A20})$$

is guaranteed by construction.

#### Appendix B: Algorithmic Details of the Ewald Attention Module

This appendix specifies the Ewald attention module introduced in the main text. The module takes E(3)-equivariant node features  $\{\mathbf{h}_i\}_{i=1}^N$  produced by short-range message passing, extracts long-range correlations

in reciprocal space, and outputs (i) updated long-range node features  $\mathbf{h}_i^{\text{lr}}$ , (ii) effective ionic charges  $Q_i$ , and (iii) orbital-projected weight matrices  $W_{i,\mu\nu}$ , which are substituted into Eq. (3) to yield  $H_{\text{lr}}$ . The computation proceeds in five stages: reciprocal-grid setup (Sec. B1), equivariant feature projection (Sec. B2), rotary position encoding (Sec. B3), linearized aggregation and feature update (Sec. B4), and decoding and  $H_{\text{lr}}$  assembly (Sec. B5).

Throughout, we adopt the following notation:  $N$  is the number of atoms in the periodic cell,  $\boldsymbol{\tau}_j$  the position of atom  $j$ ,  $\mathbf{C} \in \mathbb{R}^{3 \times 3}$  the real-space lattice matrix, and  $d$  the feature dimension.

### 1. Reciprocal Grid and Base Weights

The reciprocal lattice vectors are  $\mathbf{B} = 2\pi(\mathbf{C}^{-1})^\top$ . We enumerate all reciprocal-lattice points satisfying  $0 < |\mathbf{k}_m| < k_c$  to form the discrete wave-vector set  $\mathcal{K} = \{\mathbf{k}_m\}_{m=1}^M$ , where  $k_c$  is determined by an energy cutoff  $E_{\text{cut}}$ .

Each wave vector carries a scalar base weight  $w(\mathbf{k}_m)$  that modulates its contribution to the attention. We support two choices:

$$w(\mathbf{k}_m) = \begin{cases} \frac{1}{|\mathbf{k}_m|^2} \exp\left(-\frac{\sigma^2|\mathbf{k}_m|^2}{2}\right), & \text{(Ewald)} \\ \text{Softplus}(\text{MLP}(|\mathbf{k}_m|^2)), & \text{(adaptive)} \end{cases} \quad (\text{B1})$$

where  $\sigma$  is the Gaussian smoothing width. The Ewald form reproduces the standard reciprocal-space kernel; the adaptive form allows the network to learn  $|\mathbf{k}|$ -dependent modulations while remaining positive by construction.

### 2. Equivariant Feature Projection

A central design requirement is that the attention module preserves E(3) equivariance end to end. We achieve this by separating the roles of queries/keys (which determine *how much* information flows) from values (which carry *what* information flows):

- **Queries and keys** are derived from the *invariant* ( $l = 0$ ) scalar component  $\mathbf{x}_j^{(0)}$  of the equivariant node feature  $\mathbf{h}_j$ :

$$\mathbf{q}_j = \text{SiLU}(\mathbf{x}_j^{(0)} \mathbf{W}_Q), \quad \mathbf{k}_j = \text{SiLU}(\mathbf{x}_j^{(0)} \mathbf{W}_K), \quad (\text{B2})$$

with learnable matrices  $\mathbf{W}_Q, \mathbf{W}_K \in \mathbb{R}^{d_0 \times d}$  and SiLU activation for improved expressiveness and numerical stability under subsequent rotary encoding. Because  $\mathbf{q}_j$  and  $\mathbf{k}_j$  depend only on scalars, they are invariant under rotation and can be freely combined with position-dependent phases (Sec. B3) without breaking equivariance.

- **Values** are taken directly from the full equivariant feature:  $\mathbf{v}_j = \mathbf{h}_j$ . No position encoding is applied to values, so their equivariant transformation properties are preserved throughout aggregation.

This separation ensures that attention weights are rotationally invariant scalars, while the aggregated output inherits equivariance from the value channel alone.

### 3. Rotary Position Encoding and Ewald Phase Recovery

To inject spatial information into the attention weights, we apply rotary position encoding (RoPE) [21] to queries and keys, extending RoPE from discrete sequence positions to continuous real-space phases defined by the reciprocal lattice.

*a. Definition.* For each atom  $j$  and wave vector  $\mathbf{k}_m$ , we define the scalar phase  $\theta_{j,m} = \mathbf{k}_m \cdot \boldsymbol{\tau}_j$ . The feature vector of even dimension  $d$  is partitioned into  $d/2$  two-dimensional blocks, each rotated by  $\theta_{j,m}$ . Concretely, the block-diagonal rotation matrix  $\mathbf{R}^d(\theta) = \text{diag}(\mathbf{R}(\theta), \dots, \mathbf{R}(\theta))$  with  $2 \times 2$  blocks

$$\mathbf{R}(\theta) = \begin{pmatrix} \cos \theta & -\sin \theta \\ \sin \theta & \cos \theta \end{pmatrix} \quad (\text{B3})$$

is applied to produce encoded queries and keys:

$$\tilde{\mathbf{q}}_{j,m} = \mathbf{R}^d(\theta_{j,m}) \mathbf{q}_j, \quad \tilde{\mathbf{k}}_{j,m} = \mathbf{R}^d(\theta_{j,m}) \mathbf{k}_j. \quad (\text{B4})$$

All  $d/2$  blocks share the same physical phase  $\theta_{j,m}$ , because  $\mathbf{k}_m \cdot \boldsymbol{\tau}_j$  is a single scalar. Equivalently, each 2D block can be viewed as multiplying the complex number  $q_{j,1} + i q_{j,2}$  by  $e^{i\theta_{j,m}}$ .

*b. Sign convention.* Both queries and keys use the *same* sign for the phase angle. This choice is essential: if one were to negate the phase for keys (as in some RoFormer variants), the resulting inner product would depend on  $\mathbf{k}_m \cdot (\boldsymbol{\tau}_i + \boldsymbol{\tau}_j)$ , which is *not* translationally invariant and does not match the Ewald pairwise structure.

*c. Recovery of the Ewald relative phase.* The inner product of encoded query and key evaluates to

$$\langle \tilde{\mathbf{q}}_{i,m}, \tilde{\mathbf{k}}_{j,m} \rangle = \mathbf{q}_i^\top \mathbf{R}^d(\theta_{j,m} - \theta_{i,m}) \mathbf{k}_j, \quad (\text{B5})$$

where we used the orthogonality  $\mathbf{R}^d(\theta)^\top = \mathbf{R}^d(-\theta)$ . The effective rotation angle is

$$\theta_{j,m} - \theta_{i,m} = \mathbf{k}_m \cdot (\boldsymbol{\tau}_j - \boldsymbol{\tau}_i) = -\mathbf{k}_m \cdot (\boldsymbol{\tau}_i - \boldsymbol{\tau}_j), \quad (\text{B6})$$

so the inner product reduces to a linear combination of  $\cos[\mathbf{k}_m \cdot (\boldsymbol{\tau}_i - \boldsymbol{\tau}_j)]$  and  $\sin[\mathbf{k}_m \cdot (\boldsymbol{\tau}_i - \boldsymbol{\tau}_j)]$ , with coefficients determined by components of  $\mathbf{q}_i$  and  $\mathbf{k}_j$  in each 2D block. This is precisely the relative-displacement phase  $\mathbf{k}_m \cdot (\boldsymbol{\tau}_i - \boldsymbol{\tau}_j)$  that appears in the pairwise expansion of Eq. (3) [cf. Eq. (A14)], confirming that the RoPE-based attention kernel reproduces the Ewald summation phase structure while respecting translational invariance.

#### 4. Linearized Aggregation and Feature Update

*a. Reciprocal-space context matrix.* Standard all-pairs attention scales as  $\mathcal{O}(N^2)$ . We instead adopt linearized attention, factorizing the computation as  $\mathbf{Q}(\mathbf{K}^\top \mathbf{V})$ , which reduces the cost to  $\mathcal{O}(N)$  per wave vector and  $\mathcal{O}(N|\mathcal{K}|)$  overall.

For each  $\mathbf{k}_m$ , we first aggregate all atoms into a global context matrix  $\mathbf{C}_m \in \mathbb{R}^{d \times d_v}$ :

$$\mathbf{C}_m = \frac{w(\mathbf{k}_m)}{N} \sum_{j=1}^N \tilde{\mathbf{k}}_{j,m} \otimes \mathbf{v}_j, \quad (\text{B7})$$

where  $w(\mathbf{k}_m)$  is the base weight [Eq. (B1)] and the outer product  $\tilde{\mathbf{k}}_{j,m} \otimes \mathbf{v}_j$  contracts over the key dimension while retaining equivariant structure in the value dimension.

*b. Per-node feature extraction.* Each atom  $i$  retrieves its long-range feature by contracting its query with the context matrices and summing over wave vectors:

$$\mathbf{h}_i^{\text{lr}} = \frac{1}{\sqrt{d}} \sum_{\mathbf{k}_m \in \mathcal{K}} \mathbf{C}_m^\top \tilde{\mathbf{q}}_{i,m}, \quad (\text{B8})$$

with the standard  $1/\sqrt{d}$  scaling. Because the contraction  $\mathbf{C}_m^\top \tilde{\mathbf{q}}_{i,m}$  involves an invariant query and the equivariant value content stored in  $\mathbf{C}_m$ , the output  $\mathbf{h}_i^{\text{lr}}$  inherits E(3) equivariance from the value channel.

Note that the attention weight in Eq. (B7) uses only the base weight  $w(\mathbf{k}_m)$  and does not depend on the charge-dependent structure factor  $S(\mathbf{k}_m)$ . The module thus serves as a *feature extractor*: it produces long-range-aware node representations from which charges and weight matrices are decoded in a subsequent step (Sec. B5).

*c. Gated residual connection.* The short-range and long-range channels are fused via a gated residual:

$$\mathbf{h}_i^{\text{lr}} \leftarrow (1 - \alpha) \mathbf{h}_i^{\text{sr}} + \alpha \text{EquivariantNonlin}(\mathbf{h}_i^{\text{lr}}), \quad (\text{B9})$$

where  $\alpha \in [0, 1]$  is a learnable scalar gate initialized near zero. This design mirrors the energy decomposition  $E_{\text{tot}} = E_{\text{sr}} + E_{\text{lr}}$  at the feature level: the short-range baseline is preserved intact while the long-range correction enters perturbatively, ensuring stable early training and automatic suppression in nonpolar systems. Because the nonlinearity acts channel-wise without mixing angular-momentum components,  $\mathbf{h}_i^{\text{lr}}$  retains E(3) equivariance.

#### 5. Decoding and $H_{\text{lr}}$ Assembly

The updated node features  $\mathbf{h}_i^{\text{lr}}$  are decoded into all quantities required by Eq. (3).

*a. Effective ionic charges.* A scalar charge  $Q_i \in \mathbb{R}$  is obtained by extracting the  $l = 0$  component of  $\mathbf{h}_i^{\text{lr}}$  followed by a linear layer. Global neutrality is enforced by a zero-mean projection:

$$\tilde{Q}_j = Q_j - \frac{1}{N} \sum_{k=1}^N Q_k. \quad (\text{B10})$$

*b. Long-range edge features.* For each pair  $(i, j)$  within the real-space neighbor cutoff, we construct edge features by concatenating the node features of both endpoints and coupling them to the spherical-harmonic embedding of the bond direction  $\hat{\mathbf{r}}_{ij} = (\boldsymbol{\tau}_j - \boldsymbol{\tau}_i)/|\boldsymbol{\tau}_j - \boldsymbol{\tau}_i|$  via a Clebsch–Gordan tensor product:

$$\mathbf{e}_{ij}^{\text{lr}} = (\mathbf{h}_i^{\text{lr}} \oplus \mathbf{h}_j^{\text{lr}}) \otimes Y^{(l)}(\hat{\mathbf{r}}_{ij}), \quad (\text{B11})$$

where  $\oplus$  denotes concatenation and  $\otimes$  the Clebsch–Gordan product coupling the irreducible representations of the node features with those of the spherical harmonics  $Y^{(l)}$ . Under rotation, both inputs transform as SO(3) irreps, and the coupling ensures that  $\mathbf{e}_{ij}^{\text{lr}}$  transforms accordingly, preserving equivariance.

*c. Weight matrices.* The orbital-projected weight matrices  $W_{i,\mu\nu}$  are decoded from node features (onsite elements with both  $\mu, \nu$  on atom  $i$ ) and edge features (offsite elements with  $\mu$  on  $i$  and  $\nu$  on neighbor  $j$ ). Both decoders respect equivariance constraints imposed by the angular-momentum quantum numbers of the orbitals.

*d. Structure factor and  $H_{\text{lr}}$ .* With  $\tilde{Q}_j$  and  $W_{i,\mu\nu}$  in hand, we compute the structure factor at each sampled wave vector,

$$S(\mathbf{k}_m) = \frac{1}{N} \sum_{j=1}^N \tilde{Q}_j \exp(i \mathbf{k}_m \cdot \boldsymbol{\tau}_j), \quad (\text{B12})$$

where the  $1/N$  prefactor renders  $S(\mathbf{k}_m)$  an intensive quantity consistent with the  $1/V$  normalization in Eq. (1). The long-range Hamiltonian correction follows by direct substitution into Eq. (3):

$$H_{\text{lr},\mu\nu} = -\frac{4\pi}{V} \sum_{0 < |\mathbf{k}_m| < k_c} \frac{e^{-\sigma^2 k_m^2 / 2}}{k_m^2} \times \text{Re} \left[ S(\mathbf{k}_m) \sum_i e^{-i \mathbf{k}_m \cdot \boldsymbol{\tau}_i} W_{i,\mu\nu} \right], \quad (\text{B13})$$

evaluated analytically once  $\tilde{Q}_j$  and  $W_{i,\mu\nu}$  are provided by the network. The total predicted Hamiltonian,

$$H_{\mu\nu} = H_{\text{sr},\mu\nu} + H_{\text{lr},\mu\nu}, \quad (\text{B14})$$

completes the dual-channel pipeline.